Effect of thermal poling in sodium tantalum phosphate glass-ceramics

Gislene Batista, Thierry Cardinal, Marc Dussauze, Fabia Cassanjes, Gael Poirier

Optical Materials XXX (XXXX) XXXXXX

Contents lists available at ScienceDirect

Optical Materials

journal homepage: www.elsevier.com/locate/optmat

Research Article

Effect of thermal poling in sodium tantalum phosphate glass-ceramics

Gislene Batista [a,*], Thierry Cardinal [b], Marc Dussauze [c], Fabia Cassanjes [a], Gael Poirier [a]

[a] Grupo de Química de Materiais, Universidade Federal de Alfenas, Campus de Poços de Caldas, Poços de Caldas, MG, Brazil
[b] Institut de Chimie de la Matière Condensée de Bordeaux, Bordeaux, France
[c] Institut des Sciences Moléculaires, Bordeaux, France

ARTICLE INFO

Keywords:
Glass-ceramic
Phosphate
Tantalum
Thermal poling
Second harmonic generation

ABSTRACT

Eu^{3+}-doped sodium tantalum phosphate glass-ceramics containing bronze -like perovskite crystalline phase $Na_2Ta_8O_{21}$ were obtained with different crystalline states (degree of crystallinity and average crystallite size) by a suitable control of the heat-treatment time and temperature of the precursor glass. Luminescence properties of Eu^{3+} in these materials are in agreement with a progressive insertion of the rare earth ions in the sodium tantalate $Na_2Ta_8O_{21}$ phase, as probed by a clear decrease of the intensity ratio between transitions [$^5D_0 \rightarrow$] $^7F_2/^7F_1$ and narrowing of characteristic emission bands. Thermal poling insights were performed on these glassy and glass-ceramic materials and the experimental conditions had to be carefully optimized in the glass-ceramics to avoid electrical sparks and sample break associated with dielectric breakdown of the samples. Suitable and stable thermal poling treatments could be performed at 250 °C and 900 V under N_2 atmosphere on both glass and glass-ceramics. These first insights pointed out a lower migration kinetic of sodium ions when compared to the precursor glass as well as a lower content of depleted ions, since part of sodium is supposed to be "frozen" inside the crystalline phase in glass-ceramics. Despite these lower kinetic poling conditions, a poled sodium depleted layer whose thickness depends on the poling time was successfully formed at the anode side. Reflectance infrared spectroscopy was also used to investigate the structural changes in the poled layer. These IR data pointed out that structural changes induced by thermal poling are mainly promoted in the phosphate network rather than tantalate units in both glass and glass-ceramics in agreement with a selective sodium migration from the remaining glassy phase. Macroscopic induced SHG measured by the Maker fringes technique is also consistent with the EFISH model and quantitative simulations of these data allowed to estimate second order nonlinear optical susceptibilities $\chi^{(2)}$ ten to twenty times lower in the glass-ceramics than in the precursor glass. Such electric behavior is discussed in terms of dielectric properties of heterogeneous materials and interfacial polarization mechanisms between crystallites and glassy phase.

1. Introduction

Thermal Poling (TP) is a field assisted ion migration methodology used with several proposals in glassy materials, mainly topological modifications [1–3], differences in surface reactivity [4–6], production of masks for ion exchange [7], control of optical properties [8–10], Second Harmonic Generation (SHG) [11–13], etc. The technique consists in applying a high voltage between two sides of the heated sample, inducing the migration of the mobile ions from their original positions. During the process, mobile cations, such as Na^+, Li^+, K^+, are removed from the region under the anode by the action of the applied voltage, creating a depletion layer of a few microns. This region becomes increasingly negatively charged due to remaining NBO (Non-Bridging Oxygens) and other charge compensation mechanisms, generating a charge space orthogonally to the sample surface. When the sample is slowly cooled keeping the high voltage, the charge configuration is "frozen", and a permanent static electric field embedded under the glass surface is implanted. This permanent electric field breaks the glass centrosymmetry and allows for a second-order susceptibility $\chi^{(2)}$, which depends on the magnitude of the implanted electric field (E_{int}) and the third-order optical susceptibility ($\chi^{(3)}$) according to the relation $\chi^{(2)} = 3\chi^{(3)}E_{int}$, known as the EFISH model (Electric-Field-Induced Second Harmonic) [14–17].

Thermal poling was intensively studied in glasses and thin films with different compositions, highlighting niobium phosphate and borophosphate [18–20] or tantalum germanate glasses [9,13]. However,

* Corresponding author.
E-mail address: gislene.batista@sou.unifal-mg.edu.br (G. Batista).

the effect of thermal poling in glass-ceramics was hardly investigated, even for SHG purposes. Commonly, SHG in glass-ceramics is related to the presence of non-centrosymmetric crystalline phases embedded in the material [21–23].

Considering the lack of studies in this field, this work intended to understand the effect of thermal poling in Eu^{3+}-doped glass-ceramics containing mobile ions in both the glassy and crystalline phase and expected changes in composition and optical properties. For such purposes, Eu^{3+}-doped sodium phosphate glass samples with high Ta_2O_5 contents were investigated. In fact, previous studies have already shown that transparent glass-ceramics can be obtained in the binary system $NaPO_3$–Ta_2O_5. For high Ta_2O_5 contents, amorphous [TaO_6] agglomerates are formed in the pristine glass and act as nuclei for the crystallization of a bronze-like perovskite type crystalline phase $Na_2Ta_8O_{21}$. Therefore, at first a crystallization study was performed in a Eu^{3+}-doped sodium tantalum phosphate glass to prepare glass-ceramics with increasing crystallinity. Eu^{3+} emission spectra were used to investigate the rare earth chemical environment upon heat-treatment. Thermal poling treatments were performed on the glass and glass-ceramics and the voltage-current curves used for a better understanding of the whole migration process. Combined ToF-SIMS and SHG microscopy investigations at the anode cross-section side were used to characterize the poled depleted layer. Infrared reflectance was used to probe the structural changes after poling. Luminescence microscopy measurements were also performed to check the influence of thermal poling on the Eu^{3+} emission properties. Finally, Maker fringe measurements allowed to access the macro-SHG response of these materials after thermal poling and quantify the second order nonlinear optical susceptibilities.

2. Experimental part

Glass samples of composition 99.83 [52.5$NaPO_3$-47.5Ta_2O_5]-0.17Eu_2O_3 were prepared by weighting and grinding the starting compounds Ta_2O_5 (Alfa-Aesar 99.998 %), $NH_4H_2PO_4$ (Prolabo 99 %) and Eu_2O_3 (Acros Organics 99.99 %) in an agate mortar, heating the mixture at 1000 °C for 2 h, grinding again the treated powders and finally melting at 1615 °C for 25 min in a platinum crucible. After the melting step, the glass was obtained by cooling the crucible in cold water. The glass sample formed in the crucible was then annealed at 850 °C for 7 h in order to minimize mechanical stress resulting from thermal gradients upon cooling. Glass-ceramics (GC) were obtained by Heat-Treatment (HT) of the pristine glass at 964 °C for 30 min, 45 min, 60 min and 90 min in a Carbolite tube furnace (Table 1). Based on DSC (Differential Scanning Calorimetry) curves, this HT temperature was chosen to be 30 °C below the onset of the first crystallization event.

X-ray diffraction (XRD) were recorded in a PANalytical X'Pert Pro diffractometer using CuKα_1 radiation, in the 2θ range 8-80°. Differential Scanning Calorimetry (DSC) measurements were performed on bulk samples using a Netzsch DTA404 PC equipment, with a DSC sensor, in a platinum crucible, in two heating stages: from 40 to 600 °C with a heating rate of 20 °C.min^{-1}; and from 600 to 1200 °C with a heating rate of 10 °C.min^{-1}.

UV–visible–NIR transmission spectra were recorded between 200 and 2000 nm using a PerkinElmer Lambda 950 spectrophotometer.

In addition, photoluminescence measurements were performed in the glass and glass-ceramic powders, since europium was used as a structural probe. These measurements were performed using a Fluorolog spectrometer, front-face mode, with an integration time of 0.2s, step of 0.2 nm, entrance and exit slits of 0.25 mm; intermediate slit of 5 mm and with a 370 nm filter for the excitation spectra. Excitation spectra were obtained with an emission wavelength of 612 nm and emission spectra were obtained with an excitation wavelength of 395 nm.

For thermal poling experiments, glass and glass-ceramics samples were previously polished to a thickness of about 1 mm. Then, the sample was placed in the thermal poling cell between a cathode and an anode (Supplementary Material S1). The cathode was constituted of a n-doped silicon wafer and a 150 μm-thick borosilicate slide in contact with the sample and working as an "open" electrode for sodium migration. The anode was made of borosilicate glass slide covered with an ITO film (100 nm and 8–12 Ω/sq) in contact with the sample. The electrode had a 1 × 0.5 cm dimension and the electric contact was ensured by covering the ITO free surface and sides by chromium/gold deposition. After several vacuum purges of the poling cell, the sample was heated from room temperature to 250 °C at a heating rate of 15 °C.min^{-1} under nitrogen flow. An increasing DC voltage of 150 V min^{-1} was applied to the sample up to 900 V. As sparks related with dielectric breakdown were detected for some samples, different glass-ceramics with different crystallinities were tested and thermally poled for different times before a slow cooling to room temperature. The precursor glass was thermally poled during 30 min. Finally, the 900 V DC voltage was stopped and the sample removed from the poling cell for further characterizations. Thermally poled glass-ceramics were labeled as follows: GCX-Ymin, X being the heat treatment time at 964 °C and Y the thermal poling time at 900 V.

Sodium concentration profile under the anode was determined by Time-of-Flight Secondary Ion Mass Spectroscopy (ToF-SIMS) that were performed on a TOF-SIMS 5 - IONTOF equipment and the depth after SIMS was verified using an optical and mechanical profilometer. For sample GC30-90min, a micro-SHG mapping was recorded in backscattering mode on a modified micro-Raman spectrometer HR800 (Horiba/Jobin Yvon) using a picosecond pulsed laser at 1064 nm. Measurements were carried out on the cross-section of the poled side.

Infrared reflectance spectra were recorded on the unpoled and poled surfaces of the precursor glass and glass-ceramic GC45-10min for investigation of the structural changes induced by thermal poling. Reflectance measurements were collected in vacuum using a FT-IR spectrometer Vertex 70 V (Bruker) equipped with a Globar type source, a deuterated triglycine sulfate detector, and a mid/far infrared range beam splitter. Absorbance spectra were obtained between 150 cm^{-1} and 1300 cm^{-1} by the Kramers-Krönig analysis of the reflectance data [24]. Also, microluminescence spectra were recorded on the cross-section of the same poled glass-ceramic (GC45-10min) with a modified micro-Raman spectrometer HR800 (Horiba/Jobin Yvon) using a laser at 532 nm.

The SHG response of samples GC45-10min and GC30-90min after thermal poling was quantified using the Maker fringes technique in transmission mode. The incident laser is a 1550 nm ns laser operating at 30 Hz with a maximum pulse energy of 100 μJ during a 20 ns pulse and with a spot size of 100 μm. Two types of scans are measured with this setup. The first one is known as a θ-scan as the measurement is made as a function of incident angle (θ) with fixed incident and harmonic polarization p (horizontally) or s (vertically). The second type of scan is a ψ-scan where the incident angle is fixed to 60° and the measurement is done as a function of the polarization state of the incident beam (linear, circular, or elliptical). SHG signals are registered for both s and p polarizations (Ψs and Ψp).

Refractive indices were obtained by the Brewster angle method at 532, 639, 785 and 934 nm. Dispersion curves were obtained by fitting the experimental data with a Cauchy fit.

Table 1
Sample labels for glass-ceramics obtained by heat-treatment with corresponding degree of crystallinity and average crystal size.

Sample	Heat treatment time at 964 °C	Degree of crystallinity	Average crystallite size
GC30	30 min	25 %	10 nm
GC45	45 min	28 %	14 nm
GC60	60 min	38 %	23 nm
GC90	90 min	44 %	27 nm

3. Results and discussions

For the glass-ceramic preparation, a previous crystallization study of the pristine glass was performed. Different heat treatment times were tested at the same temperature (964 °C), which was chosen considering DSC curve of the glass presented in Fig. 1A, accordingly with glass transition temperature T_g (927 °C) and the first onset crystallization temperature T_{x1} (994 °C) values of the glass. Fig. 1A exhibits DSC curves for different GC as a function of their HT times. According to the data, the glass presented a relatively high T_g value (927 °C), related to the high connectivity of the vitreous network, with tantalum assuming a higher coordination number (clusters of [TaO_6]) acting as an intermediary between the tetrahedral phosphate units [25,26]. In fact, for this glass composition, the Ta/P atomic ratio is around 1.8. Moreover, at these high tantalum contents, these clusters act as crystallization nuclei, promoting phase separation and formation of transparent/translucent glass-ceramics [25,26]. According to the DSC curves of the GC, heat-treatments were also successful for precipitation of the crystalline phase related with the low temperature exothermic event since such event is not detected in the glass-ceramics. X-ray diffraction patterns presented in Fig. 1B also confirmed the amorphous nature of the pristine glass whereas all glass-ceramics exhibit diffraction peaks related with the bronze-like perovskite $Na_2Ta_8O_{21}$ [25–27]. Thus, it can be inferred that the low temperature exothermic event is due to this crystalline phase whereas the high temperature one still observed in GC should be related with crystallization of the remaining glassy phase. The higher crystallinity versus HT time could also be qualitatively detected by the narrower and more intense diffraction peaks for longer HT. The respective areas of diffraction peaks and diffraction halo were also integrated to determine the degree of crystallinity whereas the Scherrer equation [28] (Eq. (01)) was used to estimate the average crystal size as detailed in Table 1.

$$L = \frac{K\lambda}{\beta_{(hkl)} \cos\theta} \quad (01)$$

where K is a shape constant, assumed as 0.90 for spherical-like crystals; λ is the radiation wavelength (CuKα = 1.5406 Å); θ (rad) is half the diffraction angle (2θ) for a specific (hkl)-plane; $z_{(hkl)}$ (rad) is the corrected-peak broadening (in 2θ) arising from the nanometric size of the crystallites, and L is the crystallite size.

For Scherrer analysis, the broadening of the peaks due to microstrain is assumed to be negligible. The instrumental correction is made by means of a pattern that presents large crystals and no peak broadening from crystallites. The broadening of the peaks observed for the pattern is, therefore, almost purely instrumental. Eq. (02) is used to subtract the instrumental broadening from the total diffraction peaks broadening observed for the samples:

$$\beta_{(hkl)} = \sqrt{B^2_{(hkl)} - b} \quad (02)$$

where $B_{(hkl)}$ (rad) is the full width at half maximum of the sample peak, and b (rad) is the same parameter, but measured for the diffraction peaks of the pattern. Quartz was used as an instrumental standard for all measurements.

Transmission spectra of the precursor glass and glass-ceramics are also presented in Fig. 2, in which for the glass it is possible to observe the bands related to the Eu^{3+} ion absorptions due to the $^5L_6 \leftarrow {}^7F_0$ (395 nm) and $^5D_2 \leftarrow {}^7F_0$ (465 nm) transitions. Longer heat treatments promote a clear increasing loss of transparency at lower wavelengths attributed to scattering effects. Since the average crystallite size remains much smaller than the wavelength of incident light for all glass-ceramics, it is inferred that light scattering could be associated with a high refractive index difference between the crystals and glass host or partial agglomeration of these nanocrystals.

Furthermore, photoluminescence properties were investigated in the glass and GC samples, using europium as a structural probe. The excitation spectra are depicted in Fig. 3A with emission wavelength at 612 nm (normalized to 395 nm). As expected, the excitation spectra exhibit characteristic Eu^{3+} electronic f-f transitions, that is, from the $^7F_{0,1}$ levels to the excited states $^5D_1$ - 535 nm, $^5D_2$ - 465 nm, $^5D_3$ - 416 nm, $^5L_6$ - 395 nm, $^5G_2$ - 382nm, $^5D_4$ - 363 nm and $^5H_3$ - 320 nm. The emission spectra (Fig. 3B) with excitation wavelength at 395 nm (normalized at 591 nm) also presented the expected Eu^{3+} transitions, i.e, from the $^5D_0$ excited state to the ground states ^7F_J (J = 0,1,2,3 and 4). Moreover, the intensity ratio between electronic transitions $^5D_0 \rightarrow {}^7F_2$ and $^5D_0 \rightarrow {}^7F_1$ is related

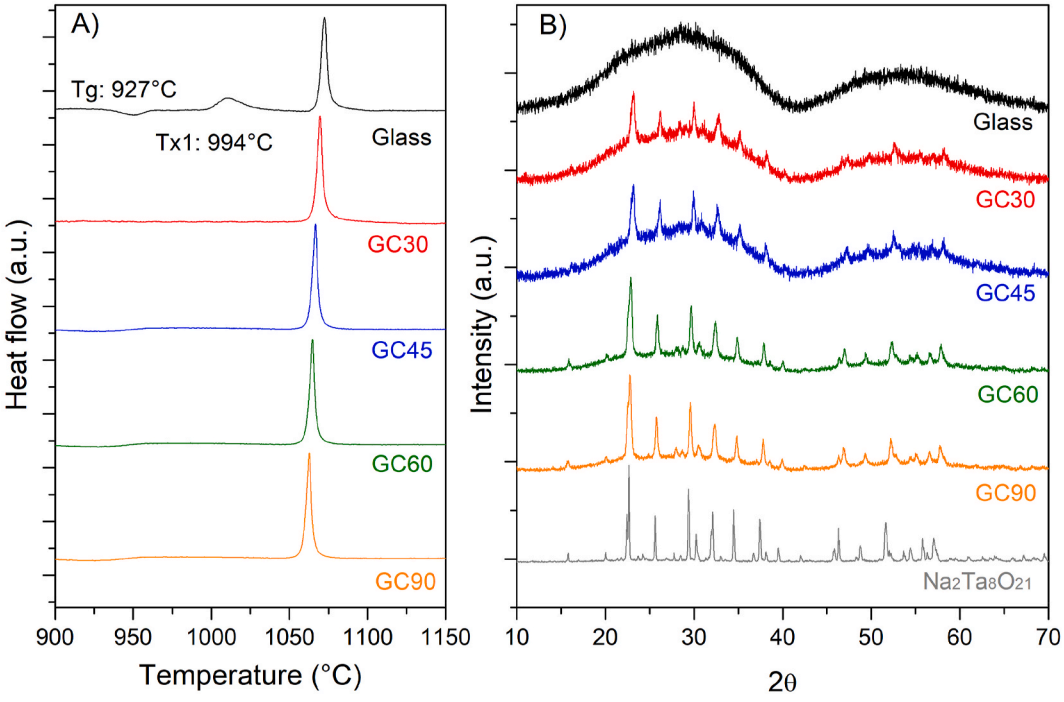

Fig. 1. A) DSC curves and (B) XRD of sodium tantalum phosphate glass and glass-ceramic samples according to heat treatment time.

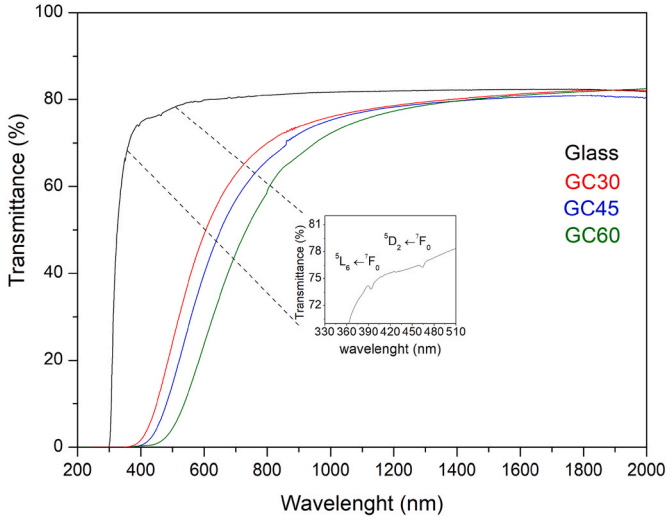

Fig. 2. Transmittance spectra of precursor glass and glass-ceramics GC30, GC45 and GC60.

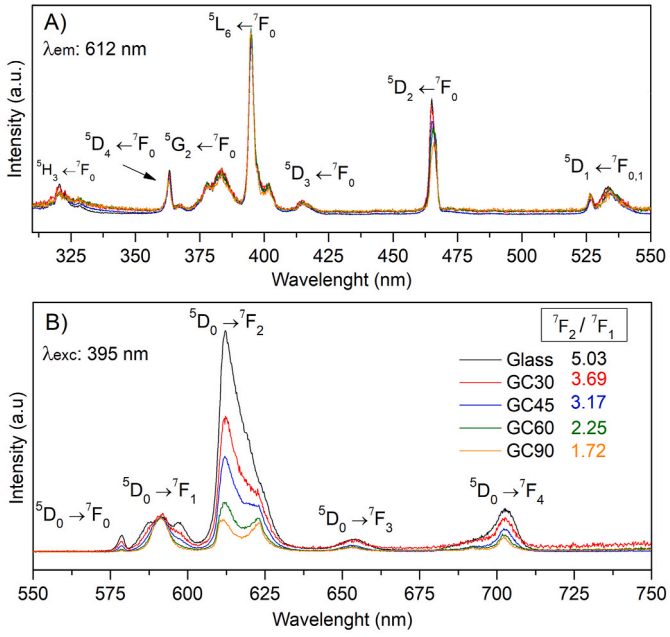

Fig. 3. Luminescence spectra of sodium tantalum phosphate glass and glass-ceramic samples according to heat treatment time: (A) excitation spectra (λ_{em} = 612 nm) and (B) emission spectra (λ_{exc} = 395 nm).

with the symmetry around Eu^{3+} ions and was useful to understand structural changes with crystallization [29]. In fact, the transition $^5D_0 \rightarrow {}^7F_1$ is a magnetic-allowed dipole transition and almost not sensitive to the Eu^{3+} near-neighbor whereas transition $^5D_0 \rightarrow {}^7F_2$, well-known in Eu^{3+} spectroscopy as the hypersensitive transition, is an electric-allowed dipole transition and its intensity is highly dependent of the symmetry. This intensity ratio, also shown in Fig. 3B, strongly decreases with increasing heat-treatment time, pointing out a much more symmetric environment around europium ions upon crystallization. Besides, $^5D_0 \rightarrow {}^7F_0$ transition around 580 nm is theoretically forbidden by the Laporte rule for both magnetic and electric dipole transitions. However, experimentally this transition is sometimes detected because of wavefunction mixing between several ^7F_n levels but is only observed if Eu^{3+} is out of an inversion center [29]. As depicted in Fig. 3B, this emission band progressively decreases with crystallization and disappears for the most crystallized glass-ceramic GC90. Finally, the Stark components of emission bands become narrower and split one another (mainly for the $^5D_0 \rightarrow {}^7F_2$ transition) as usually observed in crystalline environments. All these Eu^{3+} spectral changes with increasing crystallinity together with XRD and DSC results are a clear indication that Eu^{3+} are incorporated inside the sodium tantalate crystallites during the ceramization process.

As a first thermal poling experiment, sample GC60 was chosen to understand the overall behavior of these glass-ceramics under poling. This sample was heated to 250 °C under N_2 atmosphere and an increasing voltage was applied. However, around 900 V, the current curve suddenly "jumped" and sparks could be observed. The experiment had to be stopped and the GC sample presented a burned appearance (Supplementary Material S2). This behavior was attributed to a higher electrical conductivity of GC related with sodium tantalate crystallites when compared to the pristine glass, reaching the conditions for dielectric breakdown. For this reason, the next experiment was carried out on a less crystallized glass-ceramic GC45. Under the same experimental conditions (250 °C, 900 V, N_2), the thermal poling experiment was carried out for only 10 min and an increasing current related with charge migration was successfully detected as depicted in Fig. 4. A first interesting result was that the current did not exponentially increase and dropped when reaching the final constant voltage as observed for glasses, but kept slowly increasing during the time of treatment until heating was turned off, and then the current decreases due to decrease of temperature. Such behavior suggests a lower charge migration kinetic in GC. However, another experiment under the same conditions for 15 min resulted in the same conduction problems and sample burn. The next experiment was conducted on a less crystallized glass-ceramic GC30. Since no undesirable issue related with current jumps and sample burning were registered, thermal poling was applied for 90 min at 900 V and 250 °C. The voltage and current curves for the pristine glass, GC45-10min and GC30-90min under the same thermal poling conditions (250 °C, 900 V) are resumed in Fig. 4. The final current drop for each sample is related with the end of heating step. From the respective current curves, it clearly appears that the sodium migration mechanism and kinetic is different in the pristine glass and final glass-ceramic. In fact, the current intensity observed in a poling experiment is proportional to the density of mobile charges flowing from the anode to the cathode per time and area units. Hence, since the same anode sizes (around 0.5 cm^2) and poling conditions (250 °C, 150 V min^{-1} to 900 V) were used for both experiments, one can relate the current intensity in both cases with the quantity of Na involved in the dissociation process and migration rate from the anode to the cathode. In the case of the pristine glass and as usually observed in glasses, after reaching a threshold voltage, the current quickly increases together with the applied voltage due to the ignition of the dissociation process and subsequent higher migration rate for higher voltages [30]. After reaching a constant voltage, the current decreases because ion migration is increasingly difficulted by the formed space charge until the internal electric field reaches values close to the applied voltage. However, for GC30-90min the current increase is slower but still continues after reaching the constant voltage and remains almost constant for about 10 min before starting to decrease. Such behavior means that sodium migration is somewhat difficult in glass-ceramics because of the presence of large sodium tantalate crystallites along this migration direction. Besides, it can be inferred that lower current intensities in the glass-ceramic are related with a lower sodium content involved in this migration process, as part of sodium ions are inserted in the crystallites and are not supposed to migrate. However, other chemical analysis and structural characterizations are required to support such hypothesis.

Na^+ depletion, measured by ToF-SIMS for both thermally poled glass and glass-ceramics after different poling times, are disposed in Fig. 5A. For all thermal poling experiments, a sodium depleted layer could be identified as a sodium content decrease beneath the anode surface. However, this sodium content and depleted thickness strongly depends

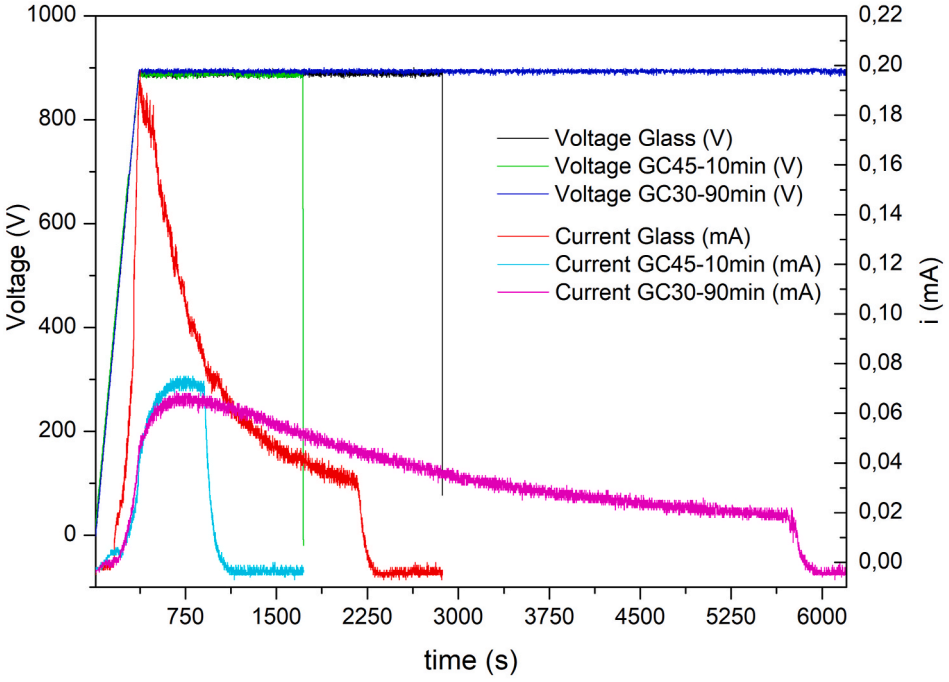

Fig. 4. Thermal poling voltage and current curves for samples treated at 250°C–900 V for the glass and glass-ceramics GC45-10min and GC30-90min.

on the sample and poling time. Optical and mechanical profilometer employed to check the depth of sodium depletion after ToF-SIMS measurements estimated poled thicknesses around 3.2 μm for GC30-90min and only 0.8 μm for GC45-10min. As expected, longer thermal poling times promote the formation of thicker depleted layers since sodium migration is a kinetic process. For the glass sample, the depleted layer is almost free of sodium as its content falls to values close to 0. However, for the glass-ceramics the depleted layer still contains a significative sodium content, in agreement with previous assumptions from current curves that only sodium ions from the remaining glassy phase are able to migrate through the vitreous network. Another detail from these ToF-SIMS data supports our migration model: besides the differences in poled layer thickness, the more crystallized glass-ceramic GC45-10min presents a higher sodium content in the depleted layer than the less crystallized one GC30-90min as can be seen at a depth of around 0.7 μm (blue arrow in Fig. 5A). Therefore, since more crystallized glass-ceramics contain more sodium ions in the crystalline phase, this result is in agreement with the assumption that such "crystalline" sodiums are not or little involved in the migration process.

Since GC30-90min was poled for a longer time, a micro-SHG profile was performed at the poled surface cross-section of this sample. As observed in Fig. 5B, a SHG signal is in fact detected beneath the anodic surface, confirming that sodium migration in glass-ceramics also promotes a charge separation, such space charge being at the origin of a static electric field orthogonal to the poled surface and mostly localized in the poled layer. Micro-SHG results also support previous thickness estimations with a poled layer thickness around 3 μm.

For a better understanding of the structural changes induced by thermal poling in both precursor glass and GC45-10min, infrared reflectance spectra were collected in both samples at the cathode and anode side (poled layer) as detailed in Fig. 6. Since infrared data are hardly found in tantalum phosphate glasses, our infrared mode attributions and structural discussion were based on niobium phosphate glasses which have already shown to give similar structural behaviors. Three main broad absorption envelopes are clearly identified between 150 and 475 cm^{-1}, 475 and 800 cm^{-1}, and 900 and 1250 cm^{-1}. The low frequency feature composed of several vibrational bands is attributed to bending modes of TaO_6 units in the tantalate network overlapped with bending modes of PO_4 units from a sodium phosphate network [31,32]. Infrared broad band between 475 and 800 cm^{-1} is mainly attributed to the tantalate network and constituted of two vibrational modes at 630 cm^{-1} and 730 cm^{-1} attributed to asymmetric stretching vibrations of Ta–O–Ta in regular and distorted 3D TaO_6 networks respectively [20,32]. For both poled glass and glass-ceramic broadening and shift to higher frequency after thermal poling is related with a stronger contribution of the stretching mode attributed to distorted TaO_6 units in the 3D TaO_6 network. Since crystallization of the $Na_2Ta_8O_{21}$ phase is not completed in this sample (Table 1) and considering that only part of sodium ions takes part in the crystallization event, it is inferred that only sodium from the remaining glassy phase is depleted in the vicinity of TaO_6 rich regions. As a result, TaO_6 octahedra from the remaining amorphous tantalate network suffer charge compensation mechanisms through progressive distortion of such units, as already described in niobium phosphate glasses for decreasing sodium contents [20]. Finally, the high frequency envelope between 900 and 1250 cm^{-1} is mainly related with the phosphate network. One can clearly see from these infrared spectra that the phosphate network is much more affected by thermal poling than the tantalate network with a relative higher intensity after treatment as well as variations of intensity ratios between the fundamental overlapped modes in this envelope. This region between 900 and 1250 cm^{-1} is mainly constituted of three contributions centered at 965, 1030 and 1120 cm^{-1}. The low and high frequency modes are related with asymmetric stretching of P–O–P bridges and terminal P–O bonds in pyrophosphate entities $P_2O_7^{4-}$ respectively. The central component at 1030 cm^{-1} is attributed to asymmetric stretching mode of isolated orthophosphate units PO_4^{3-}. It is worth noting that these entities are isolated from other phosphate chains or units but surely at least partially bonded to tantalum through P–O–Ta bridges. Based on the nominal glass composition described in the experimental section, the Na/P/Ta ratio is approximately 1/1/1.8. In this sense, pyrophosphate units can be understood as P_2O_7 entities with two NBO oxygens balanced by Na^+ and two other oxygens bonded to tantalum and are labeled $(P_2O_7)^{2-}_{2Na,2Ta}$. Following the same reasoning, orthophosphate units are supposed to be linked to one NBO and two tantalum atoms and described as $(PO_4)^{-}_{1Na,2Ta}$. For both glass and glass-ceramic

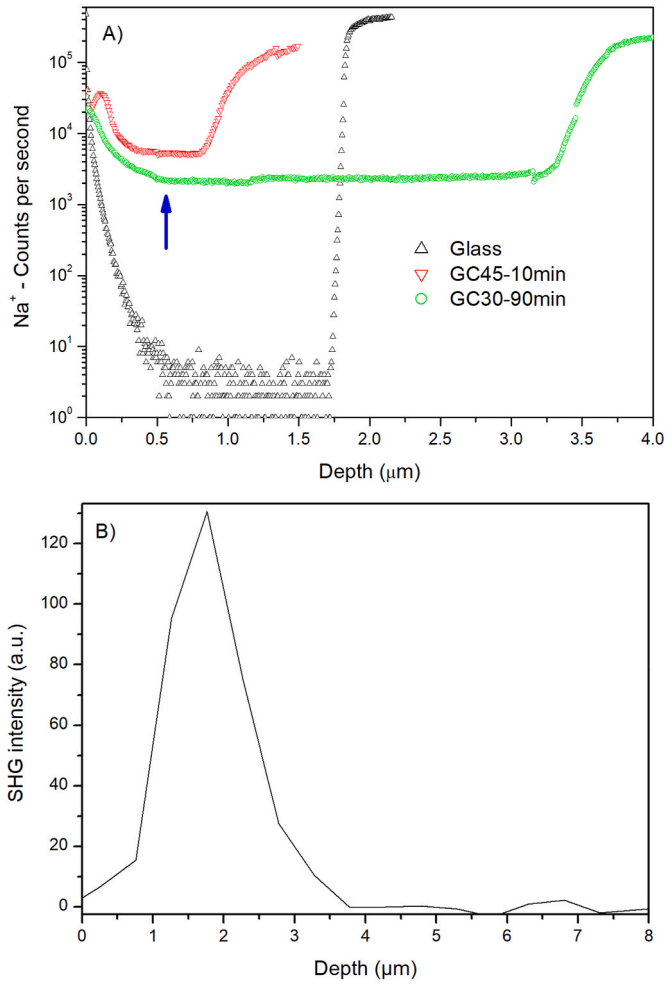

Fig. 5. A) ToF-SIMS depth profile of sodium in the precursor glass and glass-ceramics GC45-10min and GC30-90min after poling. Blue arrow indicates the difference in sodium depletion; and (B) Micro-SHG profile of sample GC30-90min at the poled surface cross-section. The 0 μm mark corresponds to the material surface at the anode side.

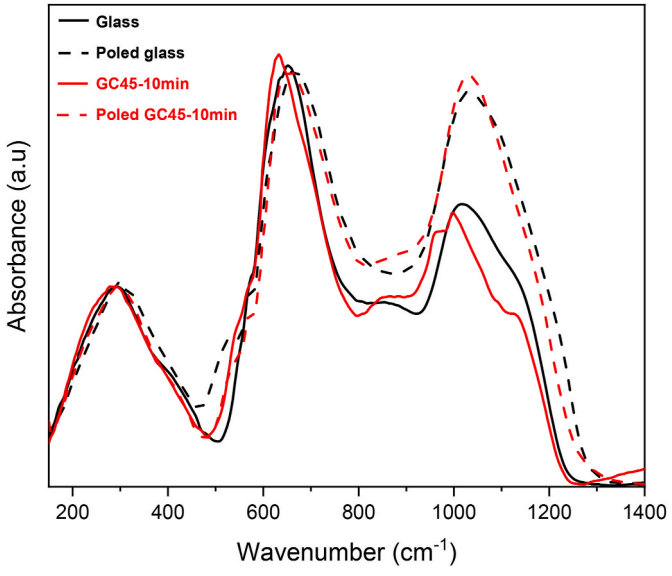

Fig. 6. Infrared absorption spectra of the glass, poled glass, glass-ceramic GC45-10min and poled glass-ceramic GC45-10min.

samples, the effect of thermal poling on the structural rearrangements in the poled layer is almost similar with a decrease in the contributions of the pyrophosphate modes and a consequent stronger contribution of the orthophosphate entities. Such behavior can be understood by the fact that sodium loss near terminal oxygens of these phosphate units must be counterbalanced by formation of more P–O–Ta bonds, converting initial $(P_2O_7)^{2-}_{2Na,2Ta}$ units in $(PO_4)_{3Ta}$ units. In fact, orthophosphate units are supposed to bond to three tantalum atoms to compensate for the sodium departure. The higher intensity ratio of the phosphate broad band in respect to the tantalate band can be understood by a higher absorption coefficient of $(PO_4)_{3Ta}$ units when compared to $(PO_4)_{1Na,2Ta}$ (Supplementary material S3). Such strong variations in the intensity ratio between these bands has also been described in niobium phosphate glasses [20]. From an overall structural description, it appears that thermal poling promotes stronger structural changes in the phosphate network, explaining the structural similarity between poled glass and glass-ceramic. Additional investigations were also conducted using Eu^{3+} as a structural probe. Microluminescence measurements were performed on the cross-section of poled glass-ceramics GC45-10min under excitation at 532 nm, in which one of the mapped spectra in depletion layer (inside poled layer) and one of the mapped spectra on the bulk area (outside poled layer) was taken for comparison (Supplementary material S4). Under these experimental conditions, it appears that Eu^{3+} emission spectra inside and outside of the poled layer are almost identical. Such result is unexpected since structural changes denoted after poling would modify europium environment. However, one should remember that sample GC45-10min is a partially crystallized glass-ceramics with part of Eu^{3+} ions already inserted in sodium tantalate crystallites whereas the others are supposed to be in a dominant amorphous tantalate environment expected to crystallize for longer heat-treatments. Since infrared data have already shown that the tantalate network is not drastically modified by poling, it can be assumed that europium ions are not affected by the structural modifications occurring mainly in the phosphate network.

The macro-SHG response of these GC materials was also investigated using the Maker Fringes setup. Fig. 7A and B refer to the SHG intensity as a function of the incident angle using a p-polarization for both the incident beam and detected SHG (θ−pp scan) for samples A) GC45-10min and B) GC30-90min. These experiments were carried out before and after thermal poling for both glasses. In fact, some glass-ceramics compositions may generate SHG signals if specific conditions i.e., the crystal phase is non-centrosymmetric [21,33] and these crystals are orientated in regions larger than the coherence length. However, the sodium tantalum phosphate glass-ceramics did not exhibit any SHG signal before poling, in agreement with luminescence data pointing out a centrosymmetric environment around Eu^{3+} inside the sodium tantalate phase. Fig. 7C and D are related with Ψ-scans experiments for which the incident angle is fixed on the sample around 60° and SHG intensity for both s and p polarizations (Ψs and Ψp) is registered as a function of the incident polarization. Both θ-scans and Ψ-scans were able to identify a SHG signal with an increasing intensity for longer poling times. Thus, one can expect that SHG is related with sodium migration and presence of the static electric field mainly implanted in the poled layer. Such electro-optical effect is known as Electric Field Induced Second Harmonic (EFISH) with its intensity governed by the second order optical susceptibility $\chi^{(2)}$, itself related to the third order optical susceptibility $\chi^{(3)}$ and the internal electric field by the relation $\chi^{(2)} = 3.\chi^{(3)}.E_{int}$. However, since other mechanisms at the origin of SHG such as molecular reorientation can take place during poling, Maker fringes data were simulated using a general matrix formulation of linear and nonlinear multilayer model [34]. In fact, in the case of a pure EFISH mechanism (i.e., SHG is only due to the static electric field implanted by thermal poling), the Nonlinear Optics (NLO) layer can be described by a $C_{\infty v}$ symmetry [35] and the associated contracted 3X6 SHG tensor contains two non-zero components $\chi^{(2)}_{zzz}$ and $\chi^{(2)}_{zxx}$ whose ratio $\chi^{(2)}_{zzz}/\chi^{(2)}_{zxx} = 3$. For this

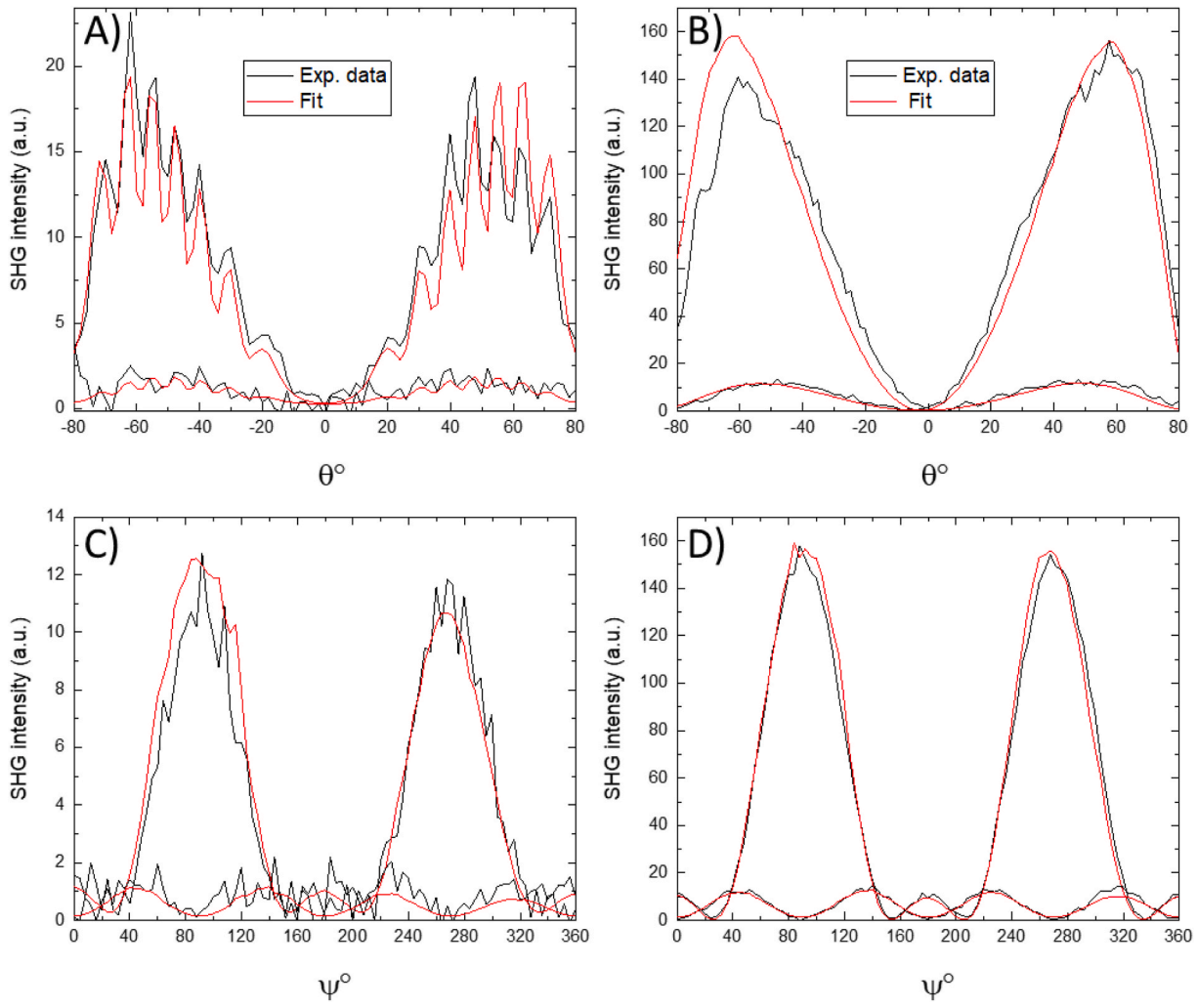

Fig. 7. Macro-SHG measurements on thermally poled glass-ceramics as a function of the incident angle with a fixed p-polarization state for both incident beam and detected SHG (θ-pp): (A) GC45-10min and (B) GC30-90min; and as a function of the polarization state of the incident beam with sample angle fixed at 60° and both s and p polarizations for the detected SHG (Ψs and Ψp): (C) GC45-10min and (D) GC30-90min.

simulation, refractive indices at the incident and SHG wavelengths were determined by the Brewster angle method whereas the poled layer thickness was extracted from the ToF-SIMS measurements (Fig. 5A). Since Maker fringes experiments were performed in transmission mode, scattering losses of glass-ceramics were also taken into account to improve the final quantitative data (Table 2). As presented in Fig. 7, fitting results on a basis of a $C_{\infty V}$ symmetry are in good agreement with experimental θ and Ψ-scans. In addition, the ratio $\chi^{(2)}_{zzz}/\chi^{(2)}_{zxx}$, which was not fixed during simulation, gives a value around 3 in agreement with an EFISH model for SHG. Finally, second-order nonlinear optical susceptibilities $\chi^{(2)}$ were extracted from these simulations as resumed in Table 2. Despite the fact that second order nonlinear optical properties could be induced in these materials through the EFISH mechanism, it appears that $\chi^{(2)}$ values are around one order of magnitude lower in glass-ceramics (0.04 p.m./V for GC45-10min and 0.016 p.m./V for GC30-90min) than in the precursor glass (0.7 p.m./V) under the same poling conditions.

To summarize, this study has pointed out three main observations regarding thermal poling of GC: (i) a decrease of the dielectric breakdown strength when the level of crystallization increase, (ii) the charge dissociation process at the anodic polarized layer, inducing sodium depletion and structural rearrangements, appears mainly within the glassy matrix and (iii) the strength of the implanted static electric field is decreased by more than one order of magnitude for the GC as compared

Table 2
Refractive indices, scattering losses at 1550 nm and 775 nm, poled layer thickness and second order non-linear optical susceptibility values at the anode and cathode sides for the precursor poled glass and poled glass-ceramics GC45-10min and GC30-90min.

Sample	Glass Na47.5TaEu-900 V		Glass Ceramic GC45-10min		Glass Ceramic GC30-90min	
n (1550 nm) ±0.01	1.87		1.98		1.98	
n (775 nm) ±0.01	1.88		2.01		2.00	
Scattering losses (1550 nm) [cm^{-1}]	–		0.09		0.06	
Scattering losses (775 nm) [cm^{-1}]	–		0.86		0.5	
L [μm]	1.53		1.25		3.19	
$\chi^{(2)}_{zzz}/\chi^{(2)}_{zxx}$	3		3		3	
$\chi^{(2)}_{zzz}$ [pm.V^{-1}]	Anode 0.7	Bulk ND	Anode 0.04	Bulk-0.002	Anode 0.016	Bulk ND

to the poled glass. To explain such observations, one should take in account the large variations of dielectric constant expected between the glassy and crystalized phases which impose to consider the GCs in this study as composite dielectric systems. In such a case, it is well known that interfacial polarization phenomena will occur and can considerably modify the dielectric properties of these inhomogeneous media as described by the Maxwell-Wagner-Sillars effect [36]. This is notably an actual subject of investigation to optimize GC properties for high energy density capacitor applications [37–40]. As observed in ferroelectric glass-ceramics, the breakdown strength decreases significantly because of interface polarization linked to high contrast of dielectric constant between the glassy and the crystallized phases [38]. Similarly, in our study, one should expect that interface polarizations promote bulk charge accumulations at each interface of the composite dielectric material which decrease drastically the breakdown strength. This has avoided to use a sufficiently high voltage during the polarization treatments of our GC samples exhibiting a degree of crystallinity above 28 %. In addition, as interfacial polarization effects promote bulk charge accumulations, this directly diminish the number of charges within the space charge layer at the anodic interface as observed with the EFISH $\chi^{(2)}$ responses lowered by more than one order of magnitude in the GC under study as compared to the homogeneous glassy material. It points out that an optimization of dielectric contrast between glassy and crystallized phases in the formulation/fabrication of GC is a key point to adapt such kind of composite dielectric materials to classical thermal poling treatments.

4. Conclusion

Eu^{3+}-doped glass samples with high tantalum contents were prepared in the binary system $NaPO_3$–Ta_2O_5 by melting around 1600 °C and quenching in the crucible. Thermal analysis together with X-ray diffraction were used to prepare glass-ceramics containing perovskite-type sodium tantalate $Na_2Ta_8O_{21}$ with different crystallinities by heat-treatments of the pristine glass. Eu^{3+} luminescence data clearly pointed out a drastic change in the Eu^{3+} environment and symmetry, in agreement with the progressive insertion of Eu^{3+} in the $Na_2Ta_8O_{21}$ crystals upon crystallization. Thermal poling experiments were performed on the glass and glass-ceramics at 250 °C and 900 V under N_2 atmosphere. Current intensity versus time during poling suggests a lower sodium migration kinetic in GC, probably related with the presence of sodium tantalate crystallites along the migration direction. Chemical analysis by ToF-SIMS demonstrated that sodium depleted layers are created under poling in the pristine glass and glass-ceramics with expected deeper depleted layers for longer poling times. However, whereas almost all sodium ions are depleted from the poled layer in the precursor glass, part of them remain in the layer in glass-ceramics, suggesting that only sodium ions from the remaining glassy phase are able to migrate during poling whereas sodium from the crystalline phase is “frozen” in the crystals. Reflectance infrared measurements on the poled and unpoled surfaces of glass and glass-ceramics were also helpful to access the main structural changes after treatment. It appears that thermal poling promotes similar structural changes in both glass and glass-ceramic occurring predominantly in the phosphate network in which it was proposed that sodium departure induces conversion of pyrophosphate units $(P_2O_7)^{2-}_{2Na,2Ta}$ to orthophosphate units $(PO_4)_{3Ta}$. On the other hand, thermal poling also promotes distortion of TaO_6 octahedra in the 3D tantalate network. SHG microscopy in the poled surface cross-section confirmed poled layer thicknesses estimated by ToF-SIMS data. Finally, macro-SHG measurements by the Maker fringe technique confirmed a SHG signal in both glass and glass-ceramics. Computational simulations also support a pure EFISH mechanism and allowed to estimate second order optical susceptibilities around 0.7 p.m./V in the glass whereas much smaller values of 0.04 and 0.016 p.m./V were found in glass-ceramics poled for 10 and 90 min respectively. To our knowledge, this is the first systematic study of the effect of thermal poling on the compositional, structural and optical properties of glass-ceramics.

CRediT authorship contribution statement

Gislene Batista: Conceptualization, Data curation, Formal analysis, Investigation, Methodology, Validation, Writing – original draft, Writing – review & editing. **Thierry Cardinal:** Conceptualization, Formal analysis, Methodology, Resources, Supervision, Validation. **Marc Dussauze:** Conceptualization, Data curation, Formal analysis, Methodology, Resources, Validation, Writing – review & editing. **Fabia Cassanjes:** Conceptualization, Investigation, Validation. **Gael Poirier:** Conceptualization, Data curation, Supervision, Validation, Writing – original draft, Writing – review & editing.

Declaration of competing interest

The authors declare that they have no known competing financial interests or personal relationships that could have appeared to influence the work reported in this paper.

Data availability

Data will be made available on request.

Acknowledgments

The authors would like to thank Brazilian Funding Agencies CNPq, FAPEMIG, CAPES and FINEP for the financial support. The infrared experiments were conducted using the SIV platform at the University of Bordeaux founded by the FEDER and the Region Aquitaine. This project has also received funding from the European Union’s Horizon 2020 research program under the Marie Skłodowska Curie grant agreement no. 823941 (FUNGLASS), New Aquitaine region (Grant 2016-1R10107) and Idex Bordeaux (Research Program GPR Light).

Appendix A. Supplementary data

Supplementary data to this article can be found online at https://doi.org/10.1016/j.optmat.2023.114734.

References

[1] H. Takagi, S. Miyazawa, M. Takahashi, R. Maeda, Electrostatic imprint process for glass, Appl Phys Express 1 (2008), 024003. https://ui.adsabs.harvard.edu/link_gateway/2008APExp...1b4003T/.
[2] A.N. Kamenskii, V. Reduto, V.D. Petrikov, A.A. Lipovskii, Effective diffraction gratings via acidic etching of thermally poled glass, Opt. Mater. 62 (2016) 250–254, https://doi.org/10.1016/j.optmat.2016.09.074.
[3] P. Brunkov, V. Goncharov, V. Melehin, A. Lipovskii, M. Petrov, Submicron surface relief formation using thermal poling of glasses, E-J. Surf Sci Nanotechnol. 7 (2009) 617–620, https://doi.org/10.1380/ejssnt.2009.617.
[4] A. Lepicard, T. Cardinal, E. Fargin, F. Adamietz, V. Rodriguez, K. Richardson, M. Dussauze, Surface reactivity control of a borosilicate glass using thermal poling, J. Phys. Chem. C 119 (2015) 22999–23007, https://doi.org/10.1021/acs.jpcc.5b07139.
[5] A. Lepicard, T. Cardinal, E. Fargin, F. Adamietz, V. Rodriguez, K. Richardson, M. Dussauze, Micro-structuring the surface reactivity of a borosilicate glass via thermal poling, Chem. Phys. Lett. 664 (2016) 10–15, https://doi.org/10.1016/j.cplett.2016.09.077.
[6] F. Lind, D. Palles, D. Möncke, E.I. Kamitsos, L. Wondraczek, Modifying the surface wetting behavior of soda-lime silicate glass substrates through thermal poling, J. Non-Cryst. Solids 462 (2017) 47–50, https://doi.org/10.1016/j.jnoncrysol.2017.02.006.
[7] E. Babich, I. Reduto, A. Redkov, I. Reshetov, V. Zhurikhina, A. Lipovskii, Thermal poling of glasses to fabricate masks for ion exchange, J Phys.: Conf. Ser. 1695 (2020), 012107, https://doi.org/10.1088/1742-6596/1695/1/012107.
[8] A. Lepicard, F. Adamietz, V. Rodriguez, K. Richardson, M. Dussauze, Demonstration of dimensional control and stabilization of second harmonic electro-optical response in chalcogenide glasses, Opt. Mater. Express 8 (2018) 1613–1624, https://doi.org/10.1364/OME.8.001613.
[9] G.Y. Poirier, L. Karam, V. Rodriguez, F. Adamietz, T. Cardinal, E. Fargin, M. Dussauze, Microscaled design of the linear and nonlinear optical properties of

tantalum germanate glasses by thermal poling, J. Mater. Chem. C (28) (2022) 10310–10319, https://doi.org/10.1039/D2TC01634F.
[10] A.L.R. Brennand, J.S. Wilkinson, Planar waveguides in multicomponent glasses fabricated by field-driven differential drift of cations, Opt Lett. 27 (2002) 906–908, https://doi.org/10.1364/OL.27.000906.
[11] G. Yang, M. Dussauze, V. Rodriguez, F. Adamietz, N. Marquestaut, K.L.N. Deepak, D. Grojo, O. Uteza, P. Delaporte, T. Cardinal, E. Fargin, Large scale micro-structured optical second harmonic generation response imprinted on glass surface by thermal poling, J. Appl. Phys. 118 (2015), 043105, https://doi.org/10.1063/1.4926866.
[12] M. Dussauze, V. Rodriguez, F. Adamietz, G. Yang, F. Bondu, A. Lepicard, M. Chafer, T. Cardinal, E. Fargin, Accurate second harmonic generation microimprinting in glassy oxide materials, Adv. Opt. Mater. 4 (2016) 929, https://doi.org/10.1002/adom.201500759.
[13] G.Y. Poirier, M. Dussauze, V. Rodriguez, F. Adamietz, L. Karam, T. Cardinal, E. Fargin, Second Harmonic Generation in sodium tantalum germanate glasses by thermal poling, J. Phys. Chem. C (123) (2019) 26528–26535, https://doi.org/10.1021/acs.jpcc.9b08221.
[14] R.A. Myers, N. Mukherjee, S.R.J. Brueck, Large 2nd-order nonlinearity in poled fused-silica, Opt Lett. 16 (1991) 1732, https://doi.org/10.1364/OL.16.001732.
[15] P.G. Kazansky, P.S.J. Russel, Thermally poled glass-frozenin electric field or oriented dipoles, Opt Commun. 110 (1994) 611, https://doi.org/10.1016/0030-4018(94)90260-7.
[16] N. Mukherjee, R.A. Myers, S.R.J. Brueck, Dynamics of second-harmonic generation in fused silica, J. Opt. Soc. Am. B 11 (1994) 665, https://doi.org/10.1364/JOSAB.11.000665.
[17] M. Dussauze, T. Cardinal, Nonlinear optical properties of glass, in: J.D. Musgraves, J. Hu, L. Calvez (Eds.), Springer Handbook of Glass, Springer International Publishing, 2019, pp. 193–225.
[18] M. Dussauze, E. Fargin, M. Lahaye, V. Rodriguez, F. Adamietz, Large second-harmonic generation of thermally poled sodium borophosphate glasses, Opt Express 13 (2005) 4064–4069, https://doi.org/10.1364/OPEX.13.004064.
[19] G. Yang, M. Dussauze, V. Rodriguez, F. Adamietz, N. Marquestaut, K.L.N. Deepak, D. Grojo, O. Uteza, P. Delaporte, T. Cardinal, E. Fargin, Large scale micro-structured optical second harmonic generation response imprinted on glass surface by thermal poling, J. Appl. Phys. 118 (2015), 043105, https://doi.org/10.1063/1.4926866.
[20] L. Karam, F. Adamietz, V. Rodriguez, F. Bondu, A. Lepicard, T. Cardinal, E. Fargin, K. Richardson, M. Dussauze, The effect of the sodium content on the structure and the optical properties of thermally poled sodium and niobium borophosphate glasses, J. Appl. Phys. 128 (2020), 043106, https://doi.org/10.1063/5.0013383.
[21] R.O. Evangelista, T. Cardinal, E. Fargin, S. Buffiere, N. Cam, M. Dussauze, V. Rodriguez, F. Adamietz, L. Marcondes, G. Batista, F.C. Cassanjes, G. Poirier, Spherulitic crystallization of quartz-like GeO_2 and correlated second harmonic generation in sodium tantalum germanate glasses, J. Alloys Compd. 877 (2021), 160245, https://doi.org/10.1016/j.jallcom.2021.160245.
[22] H. Vigouroux, E. Fargin, A. Fargues, B. Le Garrec, M. Dussauze, V. Rodriguez, F. Adamietz, G. Mountrichas, E. Kamitsos, S. Lotarev, V. Sigaev, Crystallization and Second Harmonic Generation of lithium niobium silicate glass ceramics, J. Am. Ceram. Soc. 94 (2011) 2080–2086, https://doi.org/10.1111/j.1551-2916.2011.04416.x.
[23] M. Sander, P. Engelmann, P. Jacobs, C. Roos, Controlled surface crystallization of lithium-zinc-alumosilicate glass-ceramics using thermal poling, J. Am. Ceram. Soc. 105 (2021) 3279–3290, https://doi.org/10.1111/jace.18301.
[24] E.I. Kamitsos, A.P. Patsis, M.A. Karakassides, G.D. Chryssikos, Infrared reflectance spectra of lithium borate glasses, J Non-Cryst Sol. 126 (1990) 52–67, https://doi.org/10.1016/0022-3093(90)91023-K.
[25] L.M. Marcondes, S. Maestri, B.P. de Sousa, C.R. da Cunha, R.O. Evangelista, D. Manzani, F.C. Cassanjes, G.Y. Poirier, Transparent glass and glass-ceramic in the binary system $NaPO_3$-Ta_2O_5, J. Am. Ceram. Soc. 103 (2019) 1647–1655, https://doi.org/10.1111/jace.16885.
[26] L.M. Marcondes, S.H. Santagneli, D. Manzani, F.C. Cassanjes, G. Batista, V. G. Mendoza, C.R. da Cunha, G.Y. Poirier, M. Nalin, High tantalum oxide content in Eu^{3+}-doped phosphate glass and glass-ceramics for photonic applications, J. Alloys Compd. 842 (2020), 155853, https://doi.org/10.1016/j.jallcom.2020.155853.
[27] C.R. da Cunha, L.M. Marcondes, G. Batista, R.R. Gonçalves, F.C. Cassanjes, G. Y. Poirier, Crystallization of bronze-like perovskite in potassium tantalum germanate glasses: glass ceramic preparation and its optical properties, Opt. Mater. 122 (2021), 111803, https://doi.org/10.1016/j.optmat.2021.111803.
[28] J.A. Dias, A.L.F. Freire, I. Girotto, C.D. Roveri, V.R. Mastelaro, E.C. Paris, T. R. Giraldi, Phase evolution and optical properties of nanometric Mn-doped TiO2 pigments, Mater. Today Commun. 27 (2021), 102295, https://doi.org/10.1016/j.mtcomm.2021.102295.
[29] K. Binnemans, Interpretation of europium (III) spectra - a review, Coord. Chem. Rev. 295 (2015) 1–45, https://doi.org/10.1016/j.ccr.2015.02.015.
[30] T.M. Proctor, P.M. Sutton, Static space-charge distributions with a single mobile charge carrier, J. Chem. Phys. 30 (1959) 212–220, https://doi.org/10.1063/1.1729876.
[31] E.I. Kamitsos, J.A. Kapoutsis, G.D. Chryssikos, J.M. Hutchinson, A.J. Pappin, M. D. Ingram, J.A. Duffy, Phys. Chem. Glasses 36 (1995) 141.
[32] M. Dussauze, E.I. Kamitsos, E. Fargin, V. Rodriguez, Structural rearrangements and second-order optical response in the space charge layer of thermally poled sodium-niobium borophosphate glasses, J. Phys. Chem. C 111 (2007) 14560–14566, https://doi.org/10.1021/jp074335f.
[33] T. Verbiest, K. Clays, V. Rodriguez, Second-order Nonlinear Optical Characterization Techniques: an Introduction, CRC Press, Boca Raton, 2009.
[34] V. Rodriguez, C. Sourisseau, General maker-fringe ellipsometric analyzes in multilayer nonlinear and linear anisotropic optical media, J. Opt. Soc. Am. B 19 (2002) 2650, https://doi.org/10.1364/JOSAB.19.002650.
[35] P.W. Atkins, T.L. Overton, J.P. Rourke, M.T. Weller, F.A. Armstrong, Inorganic Chemistry, Oxford University Press, Great Britain, 2010.
[36] L.K.H. Van Beek, The Maxwell-Wagner-sillars effect describing apparent dielectric loss in inhomegeous media, Physica 26 (1960) 66–68, https://doi.org/10.1016/0031-8914(60)90115-4.
[37] M.-J. Pan, E.P. Gorzkowski, B.A. Bender, C.C.M. Wu, The Effect of Interfacial Polarization on the Energy Density of Ferroelectric Glass-Ceramics, 15th Ieee International Symposium on the Applications of Ferroelectrics, Sunset Beach, NC, USA, 2006, pp. 25–28, https://doi.org/10.1109/ISAF.2006.4387824.
[38] J. Huang, Y. Zhang, T. Ma, H. Li, L. Zhang, Correlation between dielectric breakdown strength and interface polarization in barium strontium titanate glass ceramics, Appl. Phys. Lett. 96 (2010), 042902, https://doi.org/10.1063/1.3293456.
[39] X. Wang, Y. Zhang, X. Song, Z. Yuan, T. Ma, Q. Zhang, C. Deng, T. Liang, Glass additive in barium titanate ceramics and its influence on electrical breakdown strength in relation with energy storage properties, J. Eur. Ceram. Soc. 32 (2012) 559–567, https://doi.org/10.1016/j.jeurceramsoc.2011.09.024.
[40] X. Peng, Y. Pu, X. Du, J. Ji, S. Zhou, L. Zhang, The effect of glass network structure on interfacial polarization in Na2O–K2O–Nb2O5–SiO2–BaO glass-ceramics, J. Alloys Compd. 845 (2020), 155645, https://doi.org/10.1016/j.jallcom.2020.155645.